Supporting Information

Power-dependent upconversion quantum yield of $NaYF_4:Yb^{3+},Er^{3+}$ nano- and micrometer-sized particles – Measurements and simulations

Martin Kaiser,[a] Christian Würth,[a] Marco Kraft,[a] Iko Hyppänen,[b] Tero Soukka,[b] and Ute Resch-Genger[a,*]

[a] Federal Institute for Materials Research and Testing (BAM), Division Biophotonics (1.10), Richard-Willstaetter-Str. 11, D-12489 Berlin, Germany

[b] University of Turku, Department of Biotechnology, Tykistökatu 6A, Turku, FI-20520, Finland

Integrating sphere setup for absolute measurements of Φ_{UC}.

The nonlinear nature of UC emission together with the narrow absorption bands of the lanthanide ions impose stringent requirements on Φ_{UC} measurements and setup design. This includes i.) the choice of the excitation light source (high and controllable excitation power density (P) tunable over four orders of magnitude with very high stability, controlled shape of the beam profile (BP), excitation wavelength matching the maximum of the lanthanide absorption bands), ii.) the size of the measurement cell (optical path length of the beam in the sample cell, cell volume), iii.) the spatial distribution of P in the excited sample volume ($P_{BP}(x,y,z)$), and iv.) the linearity of the detection system. Our accordingly designed integrating sphere setup is illustrated in Figure S1. Its main parts are a highly stable 8 W 976 nm laser diode (wavelength stability < 0.3 nm, P stability < 0.1 % (see SI, Figure S2), collimating and focusing optics, and a laser clean filter, which is coupled via a 200 µm-sized optical fiber into a $BaSO_4$-coated integrating sphere (diameter of 15 cm) equipped with a Si-CCD detection system. To guarantee optimum excitation of the lanthanide activator ions, the intensity-weighted average emission wavelength of the laser diode was adjusted to precisely match the Yb^{3+} absorption peak at 976.4 nm (see SI, Figure S2, panel a). To realize different BPs, lenses with focal lengths of 500 mm and 125 mm were integrated into the excitation light path, yielding a Top Hat (TH; TH,exp) and a Gaussian (Gauss,exp) BP, respectively, as shown in Figure S1 (panels b) and c)) in the manuscript (see Figure 1). Two automated filter wheels equipped with reflective neutral density (ND) filters of known transmittance were placed between the laser diode and the integrating sphere. This enabled precise tuning of the average P from 0.25 – 410 Wcm^{-2} and from 2.5 - 3400 Wcm^{-2} for a TH-like beam shape and a nearly Gaussian beam shape. Φ_{UC} was obtained from the directly measured number of emitted photons per number of absorbed

photons at different P considering solely emitted photons with $\lambda < 900$ nm (integration over all UC emission bands between 370 and 890 nm). For the detection of the scattered excitation light required for calculating the number of absorbed photons in equation 2 (eq. 2) of the manuscript,[1] the intense laser light was attenuated with an absorptive ND filter (attenuation factor of ca. 5600) to prevent detector saturation.

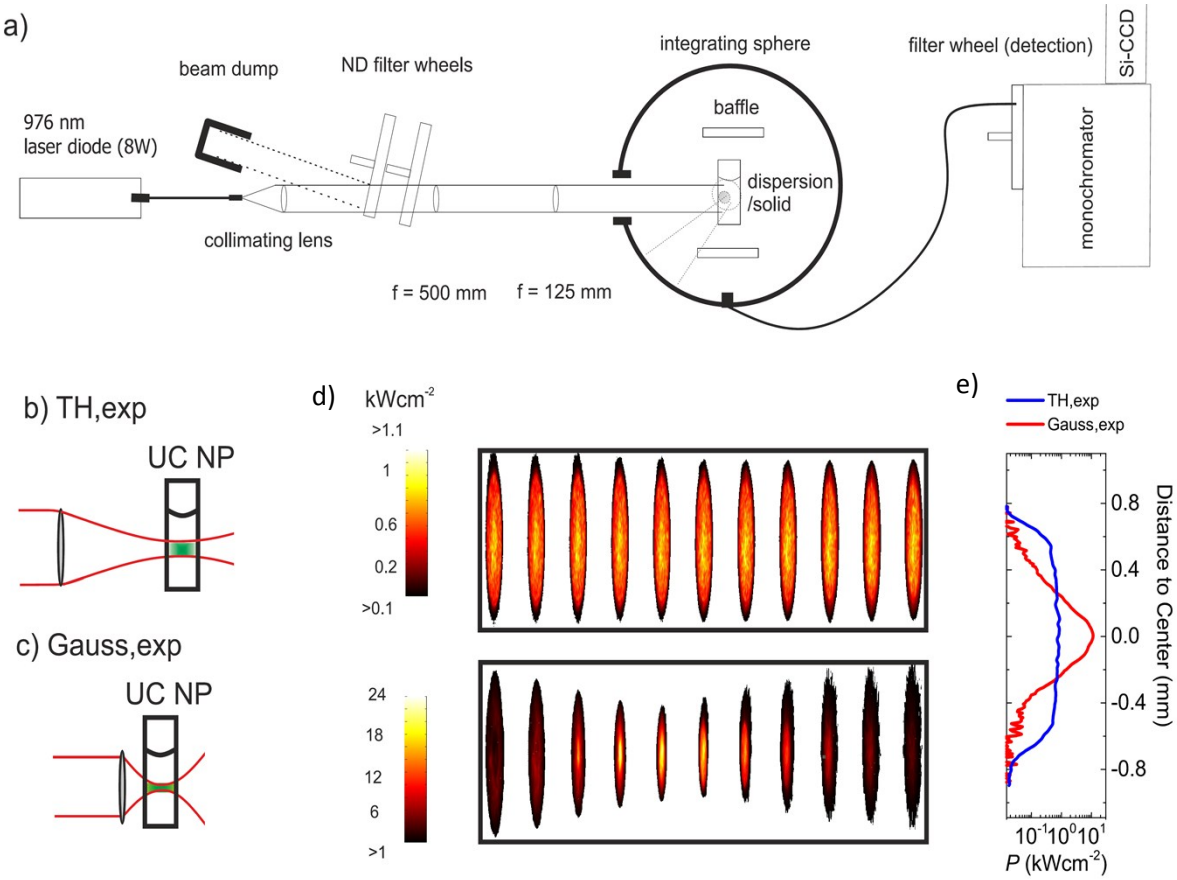

Figure S1. Schematic presentation of a) the custom-designed integrating sphere setup and the illumination geometry realized with b) a lens with a 500 mm focal length, yielding a nearly Top Hat (TH,exp) beam profile (BP) and an average beam diameter of 1.4 mm and c) a lens with a 125 mm focal length and a divergent BP yielding a nearly Gaussian BP (Gauss,exp) BP with a beam diameter of 0.55 mm; d) TH,exp (top) and Gauss,exp (bottom) PBs, determined experimentally in 1 mm steps for a path length of 10 mm; e) TH,exp and Gauss,exp averaged in the direction of the laser beam propagation (for more details, see SI, Figure S3).

Setup calibration. Calibration of the wavelength scale and range of linearity of the detection system were performed following previously described procedures.[2-4] The detection channel including the integrating sphere, optical fiber, monochromator, and detector were characterized with a calibrated spectral radiance transfer standard from 350-1050 nm using different bandpass filters and the wavelength-dependent spectral responsivities were validated with BAM spectral emission standards

F003-F005.[5] The spectral radiance transfer standard consists of a halogen lamp mounted inside an integrating sphere to guarantee a diffuse spectral radiance (Gigahertz-Optik GmbH); the wavelength dependence of the spectral radiance ($L_\lambda(\lambda)$ of this calibration lamp was calibrated by the Physikalisch-Technische Bundesanstalt (PTB). The spectrally corrected luminescence spectra/intensity values and spectral UC intensities $I_{UC}(\lambda_{em},P)$ were multiplied with λ/hc_0 to obtain spectral photon fluxes ($s^{-1}m^{-3}$) and luminescence quantum yields.[1]

Sample cells. For minimal attenuation of the laser within the sample cell, the particle concentration of the UCNP dispersion was chosen to yield an absorbance of about 0.02 at the excitation wavelength. Attenuation of P due to scattering by dispersed UCNP could be excluded (see absorption measurements shown in Figure S2). To minimize reabsorption and indirect excitation, always only a small sample volume was used. The transparent UCNP dispersions were measured in 10 mm x 4 mm quartz cuvettes (filling height of 30 mm; volume of 1200 mm³). Quartz cells filled with toluene were used as blank for UCNP dispersions and empty quartz cells for powder measurements. For measurements with powders, the particles were filled in round quartz cuvettes (volume of 2 mm³, diameter of 5 mm, perpendicular to the optical path length, optical path length of the cell of 0.1 mm) tilted by an angle of about 30° relative to the sphere entrance port to prevent loss of the first reflection of the incident excitation light.

Measurement cycles. To reduce temperature effects originating from the very intense incident laser light (see SI, Figure S13), the time for a single measurement was set to less than 30 s and a delay time between 1 and 120 s was implemented between single Φ_{UC} measurements. Furthermore, $\Phi_{UC}(P)$ was determined in duplicate, from at least two measurement cycles using an increasing and then a decreasing P.

Integration intervals. We chose the following integration intervals for the determination of the UCL intensity of the different emission bands $I_{UC}(\lambda_{em},P)$, needed for calculation of the Φ_{UC} contributions of the different UCL bands ($\Phi_{UC,\text{emission band}}$, see Table 1 and eq. 4 in the manuscript (ms): purple emission band (λ_{em} = 410 nm, $^2H_{9/2} \rightarrow {}^4I_{15/2}$): (394-430) nm), green emission bands (λ_{em} = 520 and 540 nm, $^2H_{11/2}$ and $^4S_{3/2} \rightarrow {}^4I_{15/2}$): (510-535) nm and (535-570) nm), red emission band (λ_{em} = 655 nm, $^4F_{9/2} \rightarrow {}^4I_{15/2}$): (630-685) nm) and IR emission bands ((λ_{em} = 810 nm, $^4I_{9/2} \rightarrow {}^4I_{15/2}$): (783-833) nm; λ_{em} = 850 nm, $^4S_{3/2} \rightarrow {}^4I_{15/2}$): (833-880) nm), respectively (see Figure S15)).

Beam profile (BP) characterization. The excitation beam reaching the sample was measured with a calibrated power meter. For the study of the influence of BP on resulting Φ_{UC} values, two lenses with different focal lengths were employed. BP was determined for each lens in 1 mm steps for a path length

of 10 mm using a beam profiler (Newport LBP2). The area of the excitation beam at different positions x within the beam profile (BP) was determined by integration of the beam image after subtracting the background caused by scattered laser light (see SI, Figure S2).

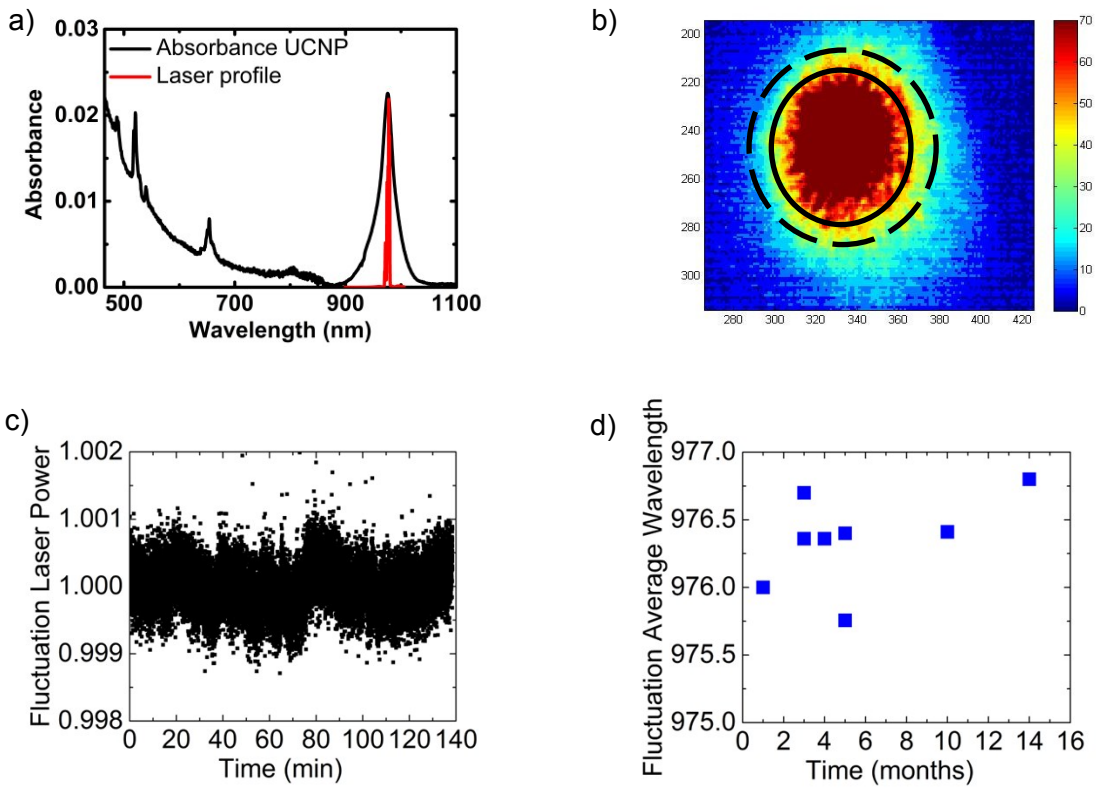

Figure S2. Top: a) Laser beam BP optimized for resonant excitation of Yb^{3+} at 976.4 nm (red line) and absorbance spectrum of the upconversion nanoparticles (UCNP) dispersed in toluene (black line) confirming the absence of particle scattering at the excitation wavelength. b) CCD image of the laser beam power distribution with the x- and y-axis given in pixels (distance between two camera pixels: 8.3 µm and 9 µm for the x- and y-axis, respectively). The solid line represents the area used for the determination of the average *P*. The dashed line illustrates the frazzling of the beam shape due to stray light. Bottom: Longterm stability of the output power of the fiber-coupled 976 nm laser diode. c) Stability of the laser diode output power measured over 2.5 hours which exceeds commonly used measurement times. d) Longterm stability of the intensity averaged emission wavelength of the laser diode controlled over a time period of 15 months. In order to ensure a high accuracy of the UC luminescence (UCL) measurements, *P* was kept constant and the attenuation was performed with reflective neutral density filters.

Table S1. Measured $\Phi_{UC,max}$ (%) and Φ_{UC} ($P_{TH,exp}$ = 20 Wcm^{-2}) of UCµP, UCNP powder, and dispersed UCNP; X represents the factor required to reach Φ_{UC} ($P_{TH,exp}$ = 20 Wcm^{-2}) of the UCµP.

	$\Phi_{UC,max}$ (%)	Φ_{UC}@20Wcm^{-2} (%)	X
UCµP as powder	10.5	10.3	1
UCNP as powder	n.d.	0.31	33
UCNP in dispersion	n.d.	0.092	112

Calculation of *P*-dependent upconversion quantum yield $\Phi_{UC}(P_{BP})$ for different beam profiles.

Figure S3 illustrates the intensity of each pixel relative to the intensity at the beam center for the y,z-plane (see Figure S1, lower panel) derived from 11 BPs recorded in 1 mm steps within the excitation light path throughout the sample. For each of these curves, i.e., for both BPs, we calculated a mean excitation power density P(x) as function of the radial distance to the beam center (x). $\Phi_{UC}(P_{BP})$ was calculated numerically for each segment with eq. S2, yielding $\Phi_{UC}(P_{BP})_{segment,l}$ values. These 11 values were then averaged (arithmetic mean) giving $\Phi_{UC}(P_{BP})$ for both BPs and a beam path length of 10 mm (see Figure S3 and eq. S1 and eq. S2).

$$\phi_{UC}(P_{BP}) = \sum_{l=0}^{10} \frac{\phi_{UC}(P_{BP})_{segment\ l}}{11} \qquad \text{(eq. S1)}$$

$$\phi_{UC}(P_{BP}))_{segment\ l} = \sum_{i} \frac{A_i(xi)\ \phi_{UC,\ sat}}{\frac{P_{balance}}{P_l(x_i)} + 1} \Big/ \sum_{i} A_i\,(x_i) \qquad \text{(eq. S2)}$$

With, $A_0 = \pi P(x_0) {x_0}^2$ and $A_i = \pi P(x_i)\left(\left(x_i\left(n + \frac{\Delta x}{2}\right)\right)^2 - \left(x_i\left(n - \frac{\Delta x}{2}\right)\right)^2\right), i > 0$,

In eq. S1 and S2, $\Phi_{UC}(P_{BP})$ segment l equals Φ_{UC} for one BP segment l (l = 0,1,2..10), $A_i(x_i)$ is the area of a pixel with excitation power density $P_l(x_i)$, and Δx presents the distance between the data points, respectively. For the simulation of $\Phi_{UC}(P_{BP})$, we used the BP data up to an radius of 0.45 mm for the Gaussian BP (Gauss,exp) and data up to a radius of 0.9 for the TH BP (TH,exp) to consider the

complete laser beam power, respectively. The $\Phi_{UC}(P_{BP})$ curves were normalized in order to fulfill the condition $\Phi_{UC}(P_{balance})=\Phi_{UC,sat}/2$.

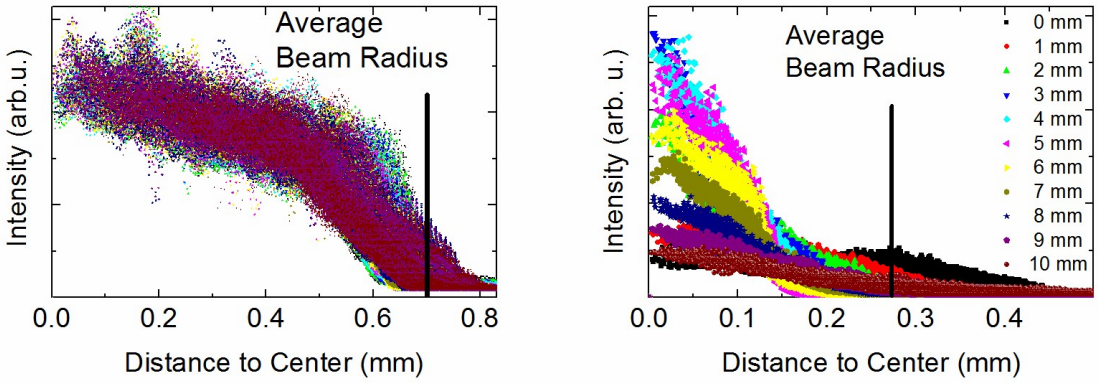

Figure S3. Intensity values of the pixels measured with a beam profiler at different distances relative to the center of the laser beam. Left: TH,exp BP, parallel beam. Right: Gauss,exp BP, divergent beam. Different colors represent here BP segments at varying distances of 0 to 10 mm along the excitation light path throughout the sample position, Figure 1S). The size of the beam diameter was defined as beam power > 4 % of the peak value (see, Figure 1S).

Fitting procedure of Φ_{UC} of the green emission band ($\Phi_{UC,green}(P)$) for UCµP and UCNP powder and UCNP in dispersion

The measured $\Phi_{UC,green}(P)$ data were fitted with a custom made data evaluation program, in which we implemented the experimentally obtained x,y,z-dependent TH,exp BP, thereby allowing the determination of the balancing power density ($P_{balance}$) and $\Phi_{UC}(P)$. These values were subsequently used for the calculation of $\Phi_{UC,green}(P)$ for the TH,ideal and Gaussian BPs with the modified Anderson Engels formula given in eq. S1.

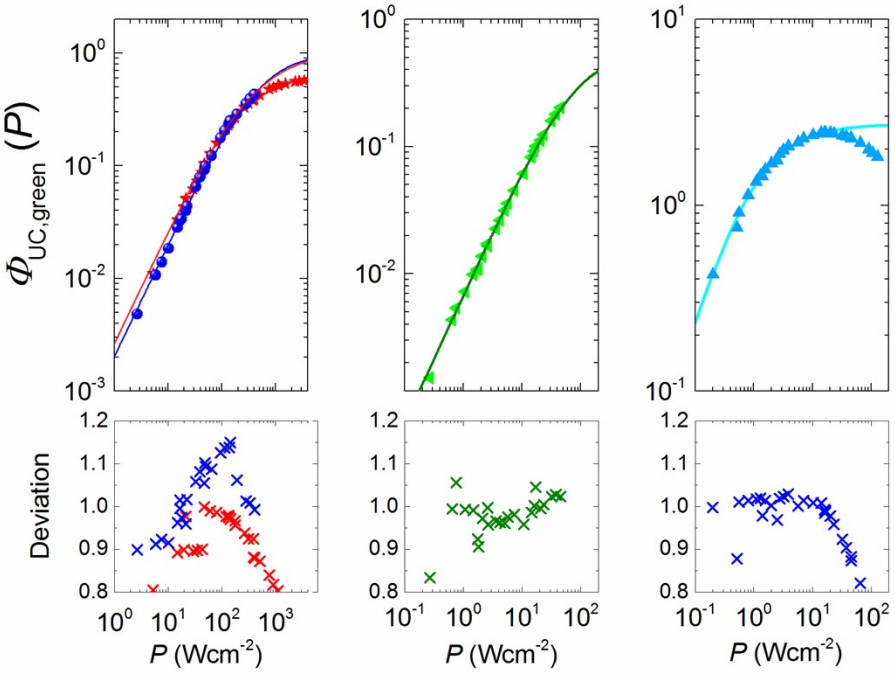

Figure S4. Measured and simulated $\Phi_{UC}(P)$ of the green emission ($\Phi_{UC,green}(P)$), derived from the sum of the integrated 520 and 540 nm emission bands, and deviation between measured and simulated $\Phi_{UC}(P)$ values for UCNP in dispersion for TH,exp (blue symbols) and Gauss,exp (red symbols) BPs (left panel), UCNP as powder (middle panel), and UCµP as powder (right panel), respectively. For powder measurements, solely a TH,exp BP was used. The fit results are summarized in Table S2.

Table S2. $\Phi_{UC,sat,green}$ and $P_{balance,green}$ values of the different UC samples obtained from fits of $\Phi_{UC,green}(P)$ shown in Figure S4.

	$\Phi_{UC,sat,green}$ (%)	$P_{balance,green}$ (Wcm^{-2})
UCµP as powder	2.7	1.2
UCNP as powder	0.6	100
UCNP dispersion	1	550

P-dependence of the absorption at 980 nm

As shown in Figure S5, we observed an increase of the fraction of photons absorbed at 980 nm with increasing *P*, followed by a diminution in absorption at 980 nm for the powders. We attribute this increase in absorption to an artefact related to a decrease of the intensity of the 980 nm emission of Yb^{3+}, lying below the scattered laser peak leading to an overestimation of the absorption factor in the order of maximum 14 % for UCµP. For the UCNP powder and UCNP dispersion, this effect is negligible, since the directly excited Yb^{3+} emission is much less pronounced due to surface quenching, as follows e.g., from its strongly reduced lifetime (reduction by a factor of about 17 compared to that of the UCµP powder, see Table S3). Such distortion was also observed by Fischer et al.,[6] leading to an overestimation of Φ_{UC} up to 60 % for core shell $NaYF_4$:Yb^{3+} ,Er^{3+} UCNPs. In our case, Φ of the Yb^{3+} emission diminishes with higher P, rendering this distortion P-dependent. The overestimation of Φ_{UC} of the UCµP of 14 % at 0.2 Wcm^{-2} is reduced to 3 % at 100Wcm^{-2}. When considering the Yb^{3+} emission, the slope of the absorption from 0.2 to 20 Wcm^{-2} disappears. The reason for the reduction in the measured absorption with increasing *P* occurring at about $P > 10$ Wcm^{-2} for the UCµP and UCNP powder is not clear yet.

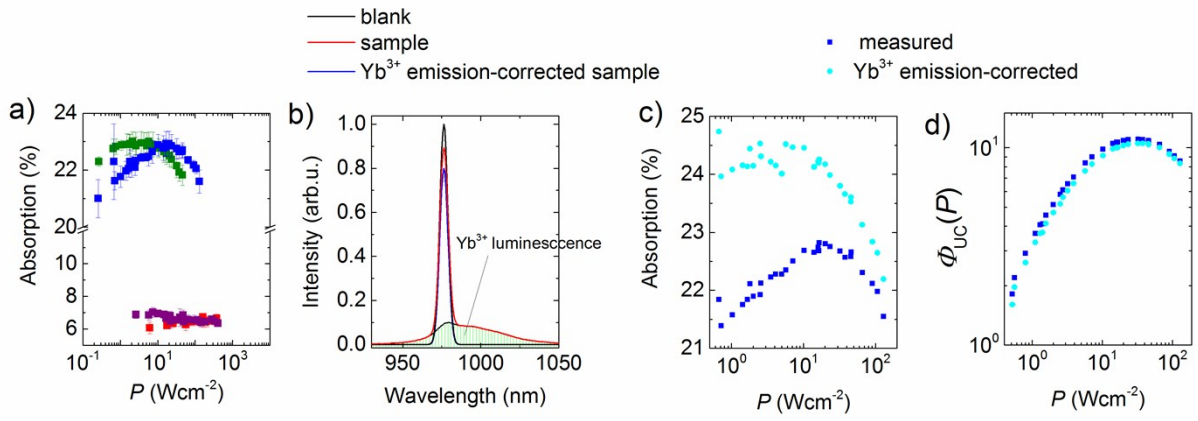

Figure S5. a) Absorption factors (given in %) of the UCµP (blue) and UCNP powder (green) as function of *P* measured with TH,exp BP and corresponding values of UCNP in toluene dispersion obtained with TH,exp (purple) and Gauss,exp (red) BP, respectively. For Gauss,exp. BP, the absorption factor UCNP dispersion were assumed to be constant for $P > 500$ Wcm^{-2}. b) Representative scheme for the correction method. c) Measured and corrected absorption values, and d) Measured and corrected Φ_{UC} values; for Φ_{UC}, also the method for correcting *P*, see Figure S8, was used.

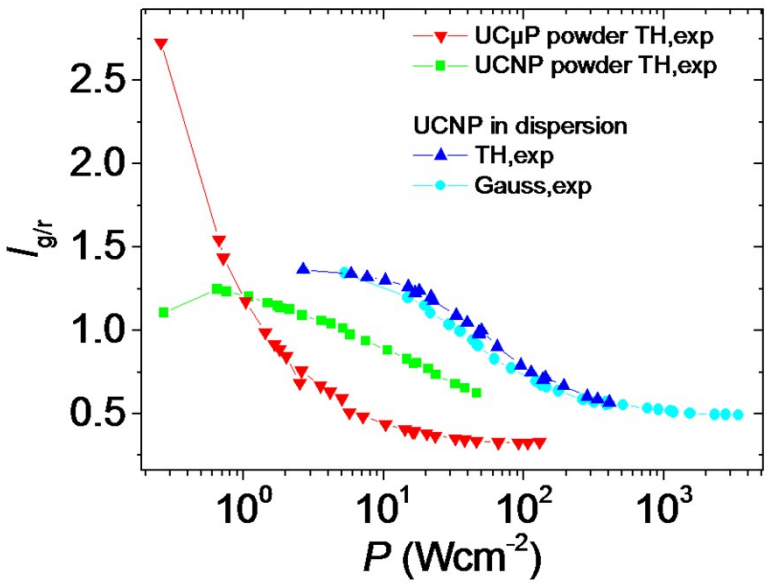

Figure S6. *P*-dependence of the green-to-red emission intensity ratio $I_{g/r}$ of the UCµP (red line) and the UCNP powder (green line) obtained with TH,exp BP and $I_{g/r}(P)$ for UCNP in toluene dispersion, measured with TH,exp (blue line) and Gauss,exp (cyan) BPs, respectively.

Determination of *P*-dependent slope factors *n*(*P*).

A linear fit method can lead to an underestimation of the slope factor n (see Figure S7), since for increasing P approaching saturation, $n(P)$ converges to 1 for a biphotonic process. UC saturation can be only accurately considered, if not a single n value of $I_{UC}(\lambda_{em},P)$ is used, but the P-dependence of n. For this purpose, $n(P)$ values are calculated here from energetically neighboring P-dependent intensity values $I_{UC,i}(\lambda_{em},P_i)$ and $I_{UC,j}(\lambda_{em},P_j)$, see eq. S4. A prerequisite for this procedure is a high stability of the excitation light source/ excitation BP and thus, also P as given here (see Figure S2, panel c)). To account for a possible deformation of the shape of the beam by the different ND filters used for controlled variation of P, we compared only $I_{UC,i}(\lambda_{em},P_i)$ values obtained with the same ND filter in the first automated filter wheel in the excitation channel.

$$n(P) = \frac{\ln I_{UC}(\lambda_{em},P_j) - \ln I_{UC}(\lambda_{em},P_i)}{\ln P_j - \ln P_i} \qquad \text{(eq. S4)}$$

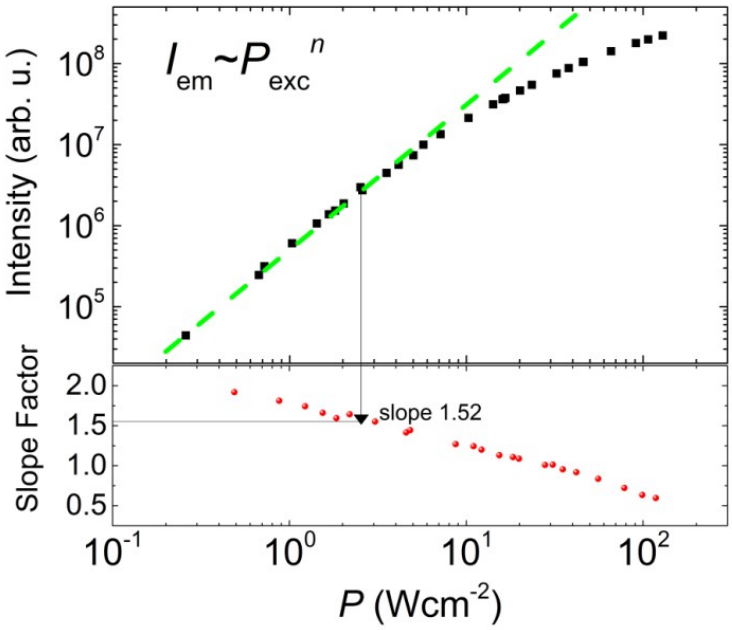

Figure S7. Top: Linear fit method used for the determination of $n(P)$ of the measured intensities (black symbols) of the different UC emission bands, here for a UCµP powder, Bottom: $n(P)$ (red symbols) values calculated with eq. S4 show that n is not constant in the studied P regime, yet depends on P.

P-Correction for UCµP Φ_{UC} data

Φ_{UC} measurement of the UCµP is distorted by the use of different reflective neutral density filters for intensity attenuation and determination of the scattering properties. Using a high reflective filter can also lead to thermal effects, i.e., inducing a change in beam shape for high laser power of 8 W. This effect was quantified by using different filter settings, yielding comparable P for the two filter wheels (see Figures S1a) and S8). As follows from this comparison, only Φ_{UC} values measured for the UCµP powder changed. The corresponding P-induced changes in Φ_{UC} of the UCµP is highlighted by changes in the relative contributions of the green and red emission intensity (see Figure 8S, left panel). These distortions were considered by shifting the Φ_{UC} values to lower P (see Figure 8S, right panel).

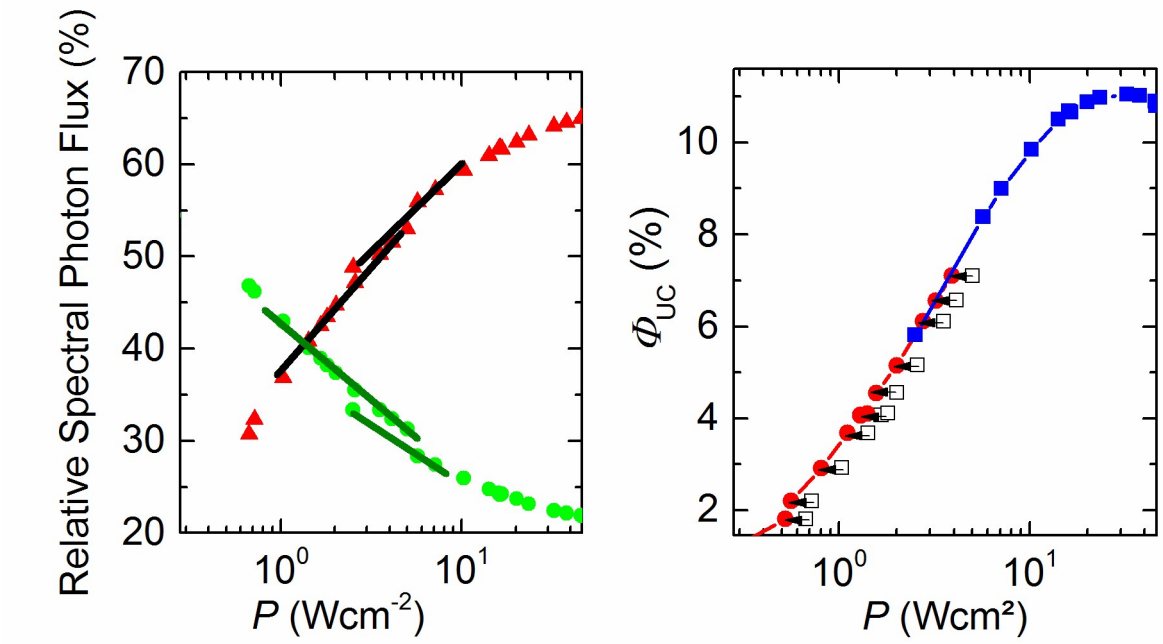

Figure S8. Left: Measured relative green and red emission intensity contributions; the lines are a guide for the eye, highlighting the *P*-induced distortions originating from different reflective filter combinations; Right: undisturbed Φ_{UC} values (blue symbols), *P*-corrected Φ_{UC} values (red symbols), uncorrected Φ_{UC} values (open symbols).

Luminescence dynamics

The UC and DC luminescence decay kinetics of the 410 nm, 540 nm, 655 nm, 976 nm, and 1520 nm emission bands of Er^{3+} and Yb^{3+} of our UC samples are summarized (Figure S9 and Table S3 and S4). Special attention was dedicated to the DC luminescence of Yb^{3+} at 976 nm ($^2F_{5/2} \rightarrow {}^2F_{7/2}$ transition; excited at 940 nm),[7] which plays a major role in the sequential UC process. Moreover, since the Yb^{3+} concentration is significantly higher than that of the sensitizer Er^{3+}, particularly the excited states of the activator ion are expected to be sensitive to surface quenching, reducing overall UC efficiency. The directly excited Yb^{3+} emission (excitation at 940 nm) of the UCµP powder decays monoexponentially with a lifetime of 2 ms, whereas the DC emission of the UCNP powder is multiexponential. The decay curves of solid and dispersed UCNP differ particularly at short times, yet converge after 0.05 ms, yielding the same longer lived emissive species (see Figure S9, panel d)). Monoexponential fitting of the tail of this decay reveals a lifetime of 0.12 ms for this longer lived species (see Table S3). At shorter times, the UCNP powder shows a short-lived luminescence component, which is absent in the case of the UCµP powder; for dispersed UCNP (see SI, Figure S9, panel d)). The short lived emissive species of the UCNP powder are ascribed to partly quenched Yb^{3+} at the particle surface quenched by surface defects and capping ligands. Oleate ligands can diminish UCL via $(CH_2)_n$ stretching vibrational modes at 2800 to 2950 cm^{-1},[8] that overlap with the energy level differences of several emission bands like the

green and red luminescence which are in the order of 3000 cm^{-1} to 3200 cm^{-1}.[8] This, together with the different Yb^{3+} decay times of the UCµP and UCNP powders of 2 ms and 0.12 ms, respectively, account for the reduction in Φ_{UC} of our UCNP. This underlines also the potential of lifetime measurements for assessing UC performance. Moreover, the decay behavior of the UCNP in the dispersed and solid state clearly correlates with the size of $P_{balance}$ of the green emission (see SI, Table S2), with a higher P being required for more strongly quenched systems to achieve a similar population of excited Yb^{3+} ions. Furthermore, a comparison of the DC and UC luminescence lifetimes of the Er^{3+} luminescence bands, which equal the intrinsic lifetime of the respective electronically excited state and reflect its prolongated through feeding from excited Yb^{3+} activator ions, reveals a decrease in prolongation factor for less efficient UCNP (see SI, Figure S9, panels a-c)).

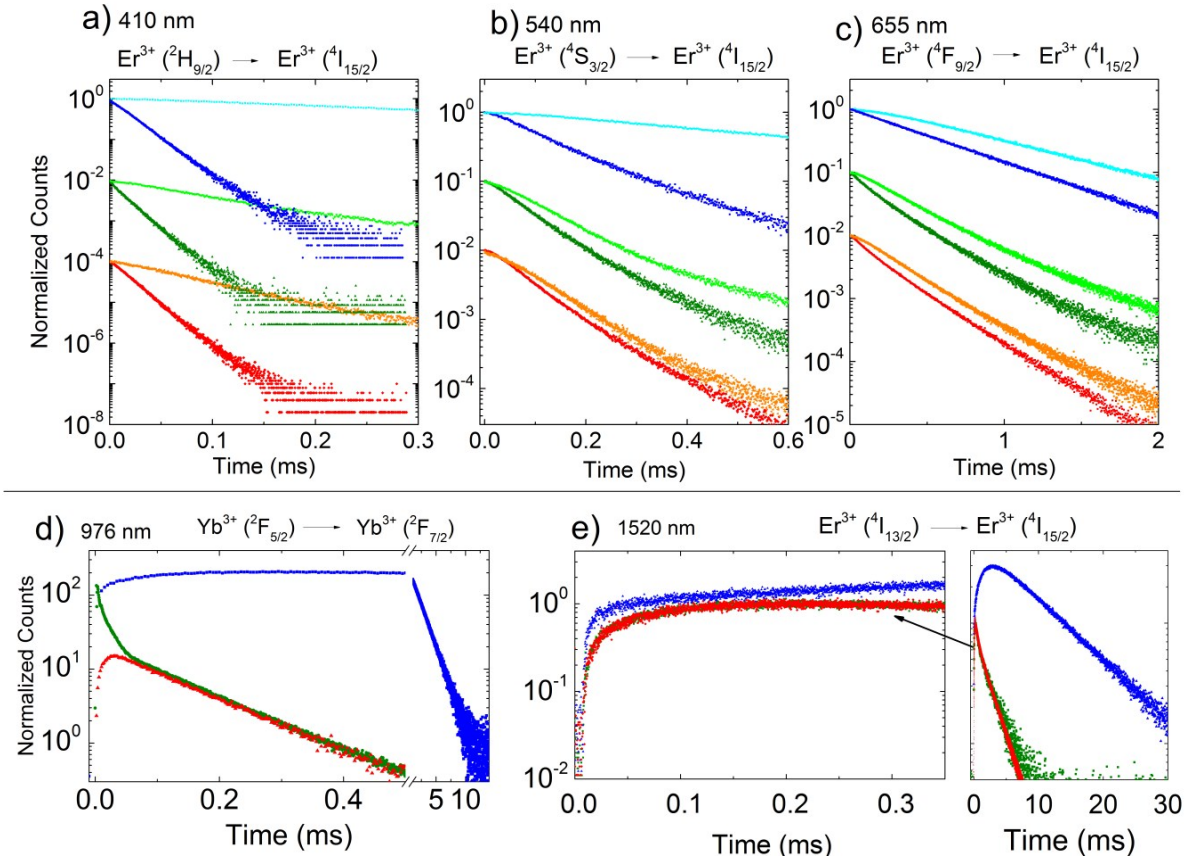

Figure S9. Decay curves originating from different energy levels of the UCµP (blue) and UCNP (green) powders and the UCNP dispersed in toluene (red), respectively. Decay behavior of a) the purple emission band of Er^{3+} ($^2H_{9/2}\rightarrow{}^4I_{15/2}$, 410 nm), b) the green emission band of Er^{3+} ($^4S_{3/2}\rightarrow{}^4I_{15/2}$, 540 nm), and c) the red emission band of Er^{3+} ($^4F_{9/2}\rightarrow{}^4I_{15/2}$, 655 nm) for λ_{exc} = 378 nm (DC emission) (dark shade of the respective color, i.e., blue, green or red) and λ_{exc} = 976 nm (UC emission) (light shade of the respective color). d) Decay of the directly excited Yb^{3+} emission ($^2F_{5/2}\rightarrow{}^2F_{7/2}$) at 976 nm obtained for λ_{exc} = 940 nm. e) Rise and decay of the Er^{3+} emission at 1520 nm ($^4I_{13/2}\rightarrow{}^4I_{15/2}$) for λ_{exc} = 976 nm measured with a short laser pulse (pulse width < 2 µs).

Method for the determination of the lifetime components.

Fitting of the lifetimes of UCNP is challenging due the complex rise and decay behavior of the emitting states and only apparent lifetimes can be obtained, which present the combined effect of energy transfer excitation and radiative decay processes of the emitting states can be obtained. Usually, a tail fit is performed since shortly after the excitation pulse, still a significant energy transfer occurs from Yb^{3+} to Er^{3+} for a short time interval, distorting fits. This can be excluded by omitting the first data points of the decay curve. Additionally, also prolongation effects on the tail of the decay curve, arising from the exceptionally slow decay processes, were removed. In order to control the quality and reliability of the lifetime values resulting from the respective fits, we determined the derivation of the decay curve $\tau_m(t)$, see equation S3. Here, I_1, I_2 and t_1, t_2 represent the neighboring intensity and time values.

$$\tau_{M(t=\frac{t_2-t_1}{2})} = \frac{t_2-t_1}{\ln(I_2) - ln(I_1)}$$

(eq. S3)

Table S3. Luminescence lifetimes of UCµP and UCNP powders and UCNP in toluene dispersion, determined for DC emission (λ_{exc} = 378 nm; excitation pulse width < 2 µs for λ_{em} =410 nm,540 and 655 nm) and UC emission (λ_{exc} = 978 nm; excitation pulse width 950 µs) and 1520 nm DC emission, respectively.

Sample	**410 nm** $^2H_{9/2} \rightarrow {}^4I_{15/2}$ **/ µs**	**540 nm** $^4S_{3/2} \rightarrow {}^4I_{15/2}$ **/ µs**	**655 nm** $^4F_{9/2} \rightarrow {}^4I_{15/2}$ **/ µs**	**980 nm** $^2F_{5/2} \rightarrow {}^2F_{7/2}$ **/ µs**	**1520 nm** $^4I_{13/2} \rightarrow {}^4I_{15/2}$ **/µs**
UCµP powder					
UC	420	660	660		
DC	19.5	185	520	2000	8500
UCNP powder					
UC	100	107	300		
DC	18	80	185	120	3000[a]
Dispersed UCNP					
UC	77	90	280		
DC	20	75	204	120	2350[a]

[a] additionally, a short lifetime component with 1300 µs (small amplitude) is observed.

Table S4. Luminescence lifetimes obtained with short pulse excitation (10 ns pulse width) at λ_{exc} = 940 nm.

Sample	**410 nm** $^2H_{9/2} \rightarrow {}^4I_{15/2}$ **/ µs**	**540 nm** $^4S_{3/2} \rightarrow {}^4I_{15/2}$ **/ µs**	**655 nm** $^4F_{9/2} \rightarrow {}^4I_{15/2}$ **/ µs**	**980 nm** $^2F_{5/2} \rightarrow {}^2F_{7/2}$ **/ µs**	**1520 nm** $^4I_{13/2} \rightarrow {}^4I_{15/2}$ **/µs**
UCµP powder					
UC	430	690	705		
UCNP powder					
UC		100			

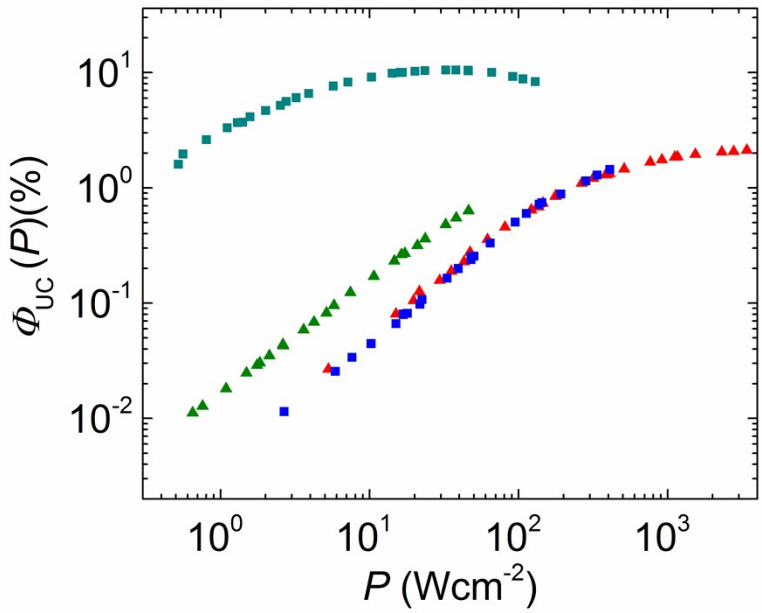

Figure S10. Comparison of $\Phi_{UC}(P)$ of the UCµP powder (dark cyan squares), UCNP powder (green triangles), and UCNP dispersed in toluene (blue squares: TH,exp BP; red triangles: Gauss,exp BP), respectively.

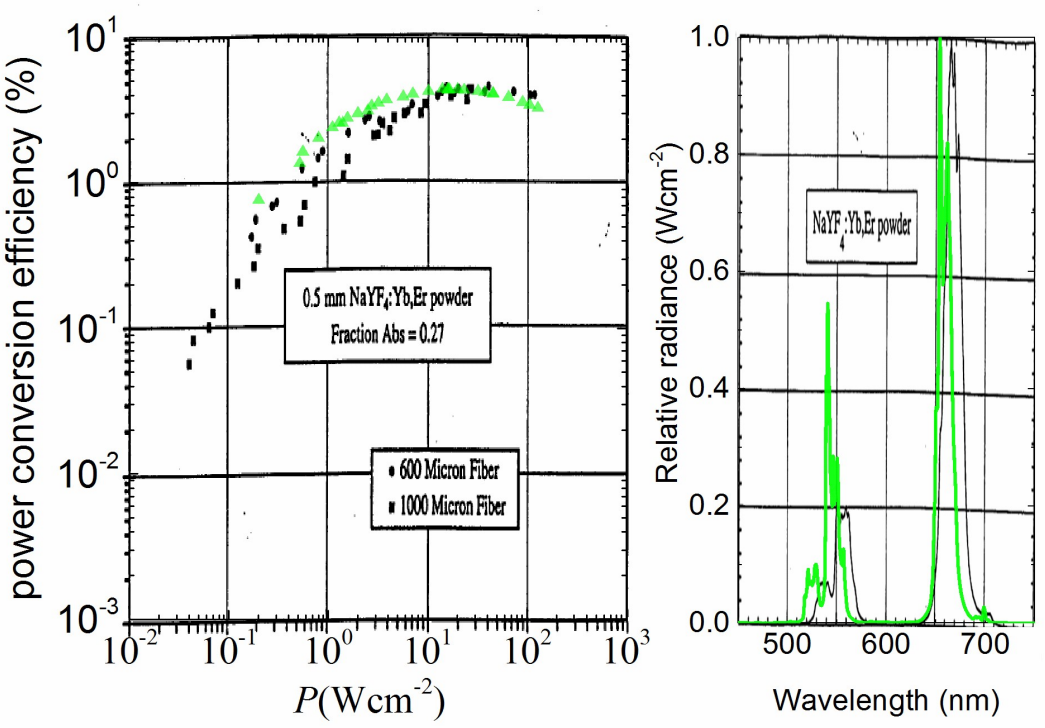

Figure S11. Left: Comparison of the green power conversion efficiency (consideration of solely the green emission), measured for UCμP (green triangles) with $\Phi_{UC,green\ and\ red}(P)$ derived from the publication of Page et al..[9]; Right: Emission spectrum of UCμP at P = 20 Wcm^{-2} (green line) and from the publication of Page[9] with no given P (have to be at least 1 Wcm^{-2}, due to the use of a 200 μm fiber for excitation). The difference between a power conversion efficiency and Φ_{UC} as defined by us in the ms in eq. 2 is that the power conversion efficiency takes the photon energy into account and can thus reach max. 100 %, whereas Φ_{UC} can reach maximally 50 % in the case of a biphotonic process and even smaller values for higher order photonic processes.

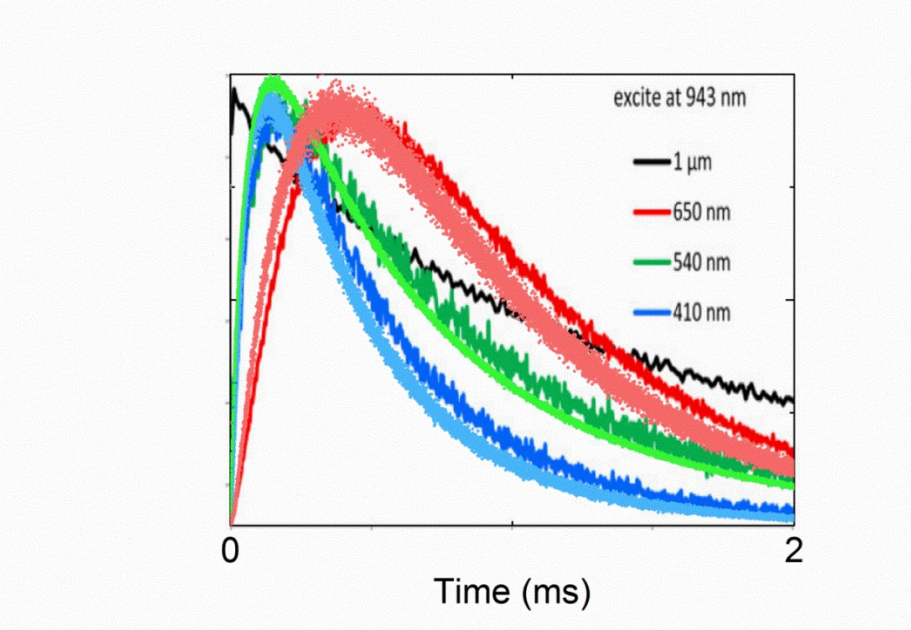

Figure S12. Comparison of the rise and decay behavior of the purple (blue), green (green), and red (red) emission of our UCµP measured with λ_{exc} = 940 nm and a pulse energy of ca. 1mJ/cm² (light colors). UCµP of the Berry group (dark colors), here using λ_{exc} = 943 nm with a pulse energy of 66 mJ/cm².

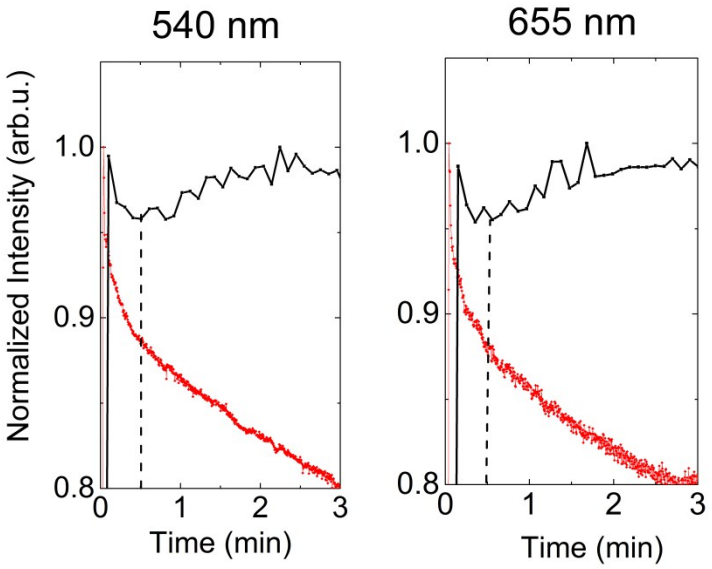

Figure S13. Integrated green (540 nm; left) and red (655 nm; right) UC emission versus illumination time (during excitation), obtained for UCµP measured as powder (black lines) for excitation with *P* of 2 W (equaling *P* of 100 W/cm²) and for dispersed UCNP (red lines) obtained for *P* of 7 W (equaling *P* of 3,400 W/cm²), respectively. The *P* values given represent the highest *P* values used for sample excitation. The measurement time was always shorter than 0.5 min in order to minimize heating effects.

Synthesis of 25 nm-sized UCNP. The synthesis of the UCNP was carried out according to Ylihärsilä et al.[10] with small modifications. In detail, methanol solutions prepared from rare earth chloride hexahydrates (0.5874 g YCl_3, 0.1583 g $YbCl_3$ and 0.0275 g $ErCl_3$ in total 12 cm^3) were added to a 500 ml flask containing oleic acid and 1-octadecene (18 and 42 cm3, respectively). The solution was then stirred and heated to 160 °C for 30 minutes and cooled down to room temperature. Then, a methanol solution containing NH_4F and NaOH (30 cm^3, 0.3574 and 0.2414 g, respectively) was added to the mixture and stirred for 30 min. at room temperature. The solution was heated to 310 °C and kept at this temperature for 1.5 hours. Subsequently, it was cooled to room temperature, the UCNP were precipitated, washed with ethanol, and separated by centrifugation. For the spectroscopic measurements, an aliquot of the purified UCNPs was dried and used as powder sample while the remaining oleic acid (OA) ligand-stabilized UCNP were dispersed in toluene.

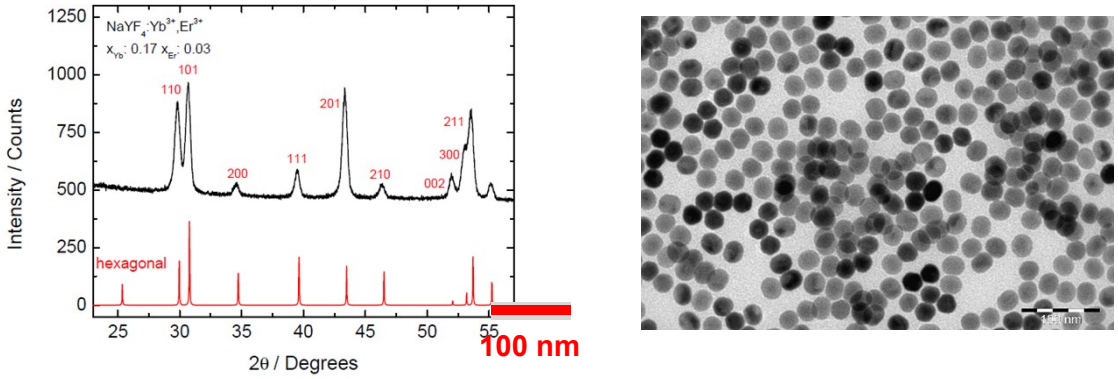

Figure S14. Left: XRD 2 theta scan, confirming the formation of hexagonal phase UCNP. Right: TEM imaging underlining a particle size of about 23 x (26-30) nm and a monodisperse particle size distribution.

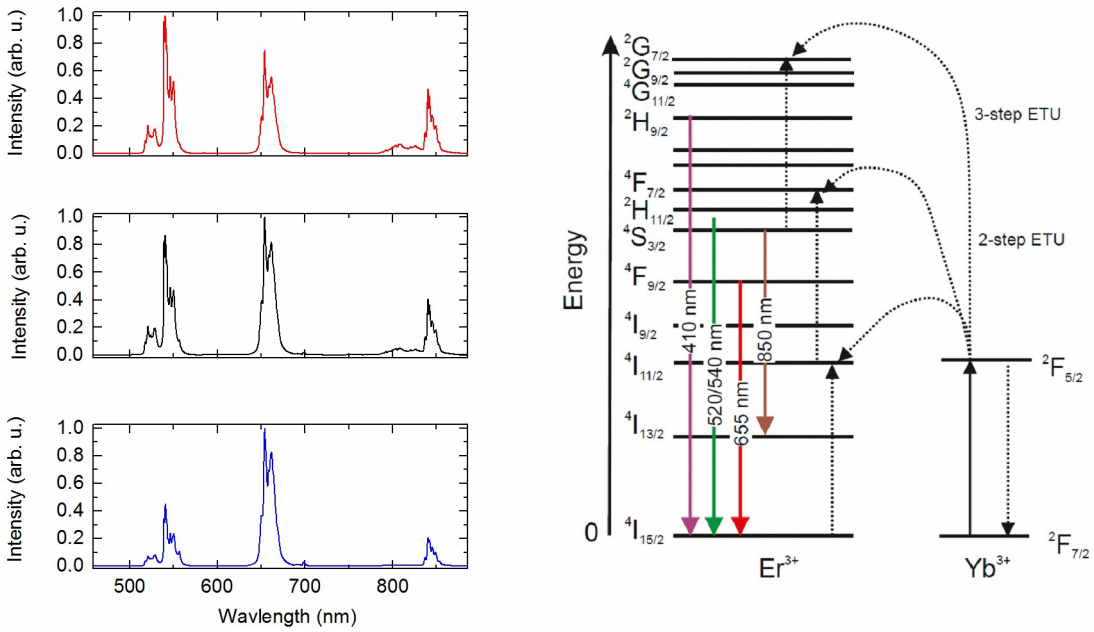

Figure S15. Left: Normalized spectrally corrected UC emission spectra for UCµP (top) and UCNP powder (middle) as well as for UCNP dispersion (bottom) for P = 20 W/cm² . Right: Energy level diagram revealing the different electronic levels of Yb^{3+} and Er^{3+} involved in excited state energy transfer upconversion (ETU) from Yb^{3+} to Er^{3+} and in the population and depopulation of the different emissive states; the dashed and solid lines represent nonradiative and radiative transitions, respectively.

REFERENCES

1. C. Würth, M. Grabolle, J. Pauli, M. Spieles and U. Resch-Genger, *Nat Protoc*, 2013, **8**, 1535-1550.
2. C. Würth, M. Grabolle, J. Pauli, M. Spieles and U. Resch-Genger, *Analytical Chemistry*, 2011, **83**, 3431–3439.
3. C. Würth, J. Pauli, C. Lochmann, M. Spieles and U. Resch-Genger, *Analytical Chemistry*, 2012, **84**, 1345-1352.
4. S. Hatami, C. Würth, M. Kaiser, S. Leubner, S. Gabriel, L. Bahrig, V. Lesnyak, J. Pauli, N. Gaponik, A. Eychmüller and U. Resch-Genger, *Nanoscale*, 2015, **7**, 133-143.
5. U. Resch-Genger, W. Bremser, D. Pfeifer, M. Spieles, A. Hoffmann, P. C. DeRose, J. C. Zwinkels, F. Gauthier, B. Ebert, R. D. Taubert, C. Monte, J. Voigt, J. Hollandt and R. Macdonald, *Analytical Chemistry*, 2012, **84**, 3889-3898.
6. S. Fischer, N. D. Bronstein, J. K. Swabeck, E. M. Chan and A. P. Alivisatos, *Nano Letters*, 2016, **16**, 7241-7247.
7. R. Arppe, I. Hyppanen, N. Perala, R. Peltomaa, M. Kaiser, C. Würth, S. Christ, U. Resch-Genger, M. Schäferling and T. Soukka, *Nanoscale*, 2015, **7**, 11746-11757.
8. S. Wu, Y. Ning, J. Chang and S. Zhang, *Journal of Luminescence*, 2013, **143**, 492-497.

9. R. H. Page, K. I. Schaffers, P. A. Waide, J. B. Tassano, S. A. Payne, W. F. Krupke and W. K. Bischel, *Journal of the Optical Society of America B-Optical Physics*, 1998, **15**, 996-1008.
10. M. Ylihärsilä, E. Harju, R. Arppe, L. Hattara, J. Hölsä, P. Saviranta, T. Soukka and M. Waris, *Clinical Microbiology and Infection*, 2013, **19**, 551-557.